Improved Estimation of Orbits and Physical Properties of Objects in GEO

Ben K. Bradley and Penina Axelrad
University of Colorado Boulder

ABSTRACT

Space-based space surveillance (SBSS) is required to observe objects in geosynchronous orbit (GEO) without weather restriction and with improved viewing geometry. SBSS satellites have thus far been placed in Sun-synchronous orbits (SSO). This paper investigates the benefits to GEO orbit determination (including the estimation of area and mass) gained by using an optical telescope placed in geosynchronous transfer orbit (GTO). Precise ephemerides of Galaxy 15 and a fictitious debris object are used with sparse, simulated astrometric and photometric measurements to analyze capabilities of a standalone GTO-based SBSS platform as well as in combination with an SSO sensor. Results show that the use of a GTO improves velocity and mass estimation as compared to an SSO. Together, the two sensor platforms significantly reduce the estimated covariance for position, velocity, area, and mass of GEO objects.

1. INTRODUCTION

Debris in geosynchronous orbit (GEO) is of particular concern because the GEO belt is such a valuable, limited resource, used by both the commercial and military sectors. Treated as a commodity, orbital slots in GEO allotted to countries and companies have a typical size of about 0.1 degrees in longitude and latitude [1, 2]. It has become common practice to place several satellites in a single slot, making accurate tracking of each satellite necessary for the safe and continued use of the GEO belt. We currently rely on ground-based optical telescopes, a few recent space-based telescopes in Sun-synchronous orbit (SSO), and owner-operator data sharing to keep track of objects in GEO [3]. However, our *tracking* capability is limited to about 1-m diameter objects and only operational spacecraft in the data sharing sense. Data from ESA's Space Debris Telescope (ESASDT), which can *detect* objects as small as 10 cm in diameter, indicates there is a substantial population of small debris in GEO [4–6].

Space-based space surveillance (SBSS) is a solution capable of detecting small debris and does not suffer from complications associated with ground-based platforms, such as weather and limited access to the GEO belt. Recent missions include SBSS Block 10, Sapphire, and NEOSSat, which are all SSO-based platforms. While optical telescopes placed in SSOs can maintain a low solar phase angle and consistent measurements, they are very far away from the GEO belt. The visibility of small debris from alternative orbits, such as geosynchronous transfer orbits (GTO) and sub-GEO orbits, has been investigated in several papers using ESA's PROOF tool [7–9]. References [10–12] demonstrate that objects down to 1-2 cm in diameter are capable of being detected by an optical sensor placed in a GTO, and [13, 14] report on the use of SSO and sub-GEO orbits for space surveillance, including an overview of the instrumentation required for these missions. The benefit of these orbits is their ability to observe GEO from a much closer distance, as depicted in Fig. 1. Based on these prior analyses of the detectable diameter of debris for various orbits and instrument configurations, our research seeks to evaluate the potential orbit determination accuracy that can be achieved with such observations.

This paper focuses on the improvement in position, velocity, area, and mass estimation gained by the use of an optical telescope placed on a GTO. Performance is investigated on a standalone basis and in combination with an SSO sensor. Publicly available ephemerides of wide area augmentation system (WAAS) satellites and simulated objects are used to simulate astrometric and photometric measurements taken by an optical sensor and then fused during filtering. Orbit determination and physical property estimation capabilities of a GTO surveillance platform are assessed and compared to an SSO sensor.

Recently, several papers have reported on simulation studies that estimate orbits and physical properties of target objects [15–21]. However, these studies exclusively use simulated objects and ground-based measurements, often with dense and long data arcs. While these simulations provide a useful bound on the levels of accuracy achievable in ideal conditions, they do not provide a meaningful result for realistic sparse data scenarios. For our first simulation, the precise WAAS ephemeris of Galaxy 15 is used during its uncontrolled period in May of 2010. WAAS ephemerides are
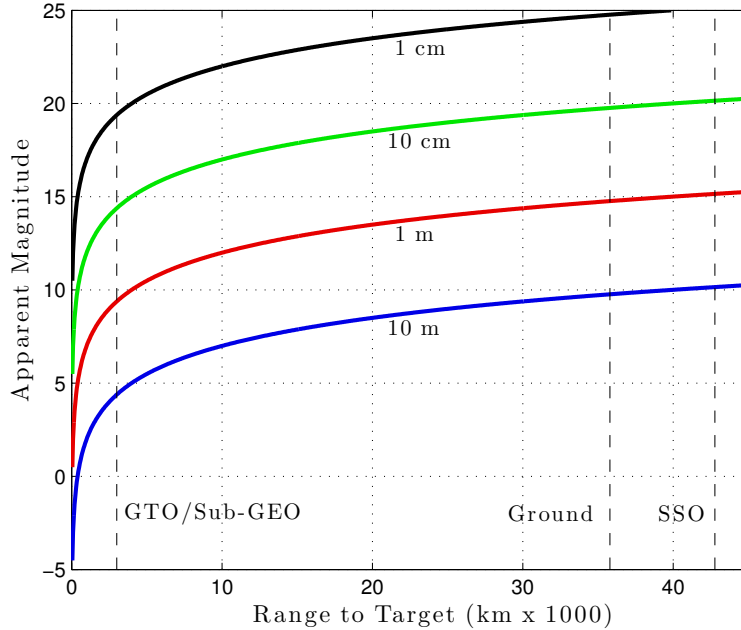
Fig. 1. Apparent visual magnitudes of objects with varying spherical diameters being observed over a range of distances. Objects are spherical in shape with a coefficient of reflectivity (C_r) of 1.2. The distance marked for GTO/sub-GEO is 3,000 km and is only an approximation to where observations will be made from.

publicly available and accurate to meter level, as demonstrated by [22]. By simulating degraded right ascension and declination observations, consistent with these ephemerides and with realistic sparse observation tracks, a more realistic assessment of potential orbit determination accuracy of SBSS systems can be achieved. This paper demonstrates that the addition of a GTO-based sensor to SSO measurements significantly improves upon the estimated covariance of position, velocity, area, and mass of GEO objects. Discussion of simulated optical measurements and results from two orbit determination simulations are included.

2. SIMULATING OPTICAL OBSERVATIONS

This section details the computation of photometric (apparent magnitude) measurements and their uncertainty based on signal-to-noise ratio (SNR) recorded by the charge-coupled device (CCD) of the telescope. The general equation for apparent magnitude is

$$m_1 = m_2 - 2.5 \log_{10}\left(\frac{f_1}{f_2}\right) \tag{1}$$

where the subscript 1 indicates the target object apparent magnitude and flux and the subscript 2 indicates the reference object apparent magnitude and flux [23]. In our case, we use the Sun as our reference object. For a spherical object, we have

$$m_v = -26.74 - 2.5 \log_{10}\left(\frac{AR_{\text{diff}}F(\phi)}{\rho^2}\right) \tag{2}$$

where -26.74 is the apparent visual magnitude of the Sun[1], A is the cross-sectional area of the sphere, R_{diff} is the diffuse reflectivity coefficient, $F(\phi)$ is the phase function, and ρ is the distance from the observer to the target object [24]. The subscript, v, for the object's magnitude specifies that we are talking about apparent "visual" magnitude, i.e. in the visual band of wavelengths. For a diffuse (Lambertian) sphere, R_{diff} is related to the coefficient of reflectivity (C_r) through $C_r = 1 + 2/3R_{\text{diff}}$ [19]. The phase function for a sphere

$$F(\phi) = \frac{2}{3\pi^2}\{(\pi - \phi)\cos(\phi) + \sin(\phi)\} \tag{3}$$

---

[1]NASA Sun Fact Sheet: http://nssdc.gsfc.nasa.gov/planetary/factsheet/sunfact.html

takes the viewing geometry into account, where ϕ is the solar phase angle (observer-target-Sun angle) [25, 26]. With the photometric measurement of apparent magnitude comes some uncertainty, σ_m. Based on [27], we approximate the magnitude uncertainty as a function of SNR

$$\sigma_m = 2.5 \log_{10} \left(1 + \frac{1}{SNR} \right). \tag{4}$$

Equation (4) is used to add zero mean Gaussian noise with standard deviation σ_m to simulated magnitude observations.

The SNR of an object on a CCD is dependent on the object brightness, sky background, as well as telescope and CCD properties such that

$$SNR = \frac{S}{\sqrt{S + S_{\mathrm{sky}} + n_{\mathrm{pix}}(RON + DC)}} \tag{5}$$

where S is the signal from the target object (in photons), S_{sky} is the sky background signal, RON is the readout noise of the CCD, DC is the dark current of the CCD, and n_{pix} is the number of pixels used to compute SNR [23, 28]. We ignore readout noise and dark current for this study since they are relatively small, and use a value of 20.7 mag/arcsec^2 for the sky brightness. The sky brightness value corresponds to 10 days from new moon in the visual band [29, 30].

The photon signal rate of the source object, S (photons), is proportional to the flux of the source f_1 (W/m^2). Equation (1) is used to compute f_1 based on the Sun as a reference with a magnitude of -26.74 and flux of 547 W/m^2. We do not use the well known "solar constant" of 1366 W/m^2 for this computation, because we are generating observations in the visible spectrum, which is approximately 40% of the total flux from the Sun [31]. This percentage, quoted by [31], can be obtained by integrating the black body curve for the Sun in the visible band.[1] The signal of the target object received by the CCD is given by

$$S = \frac{f_1}{E_{\mathrm{v}}} \frac{\pi D^2}{4} T_{\mathrm{int}} \, \eta_{\mathrm{QE}} \, \eta_{\mathrm{opt}} \tag{6}$$

where E_{v} is the energy of a photon (at a wavelength of 550 nm), T_{int} is the CCD integration time, D is the aperture diameter of the telescope, η_{QE} is the quantum efficiency of the CCD, and η_{opt} is the optical transmission.

Unfortunately, computing SNR is heavily dependent on the telescope and CCD properties, making any measurement campaign simulation slightly different depending on the hardware settings. However, [13, 14] present a recommended telescope and CCD setup for the very same type of mission being discussed in this study, a space-based telescope in a GTO observing the GEO belt. It is this setup that we use for simulating photometric measurements in Simulation 2 for both GTO and SSO sensors. Each property is listed in Table 1.

Table 1. Telescope and CCD properties for GTO and SSO observation platforms.

Property	GTO and SSO [13, 14, 28]
Field of View	6°
Aperture Diameter (D)	20 cm
Focal Length (f_{tel})	41 cm
CCD Pixel Size	18 μm (9.06 "/pix)
CCD Size	2048 × 2048 pixels
Quantum Efficiency (η_{QE})	0.80
Optical Transmission (η_{opt})	0.65
Integration Time (T_{int})	2 s

3. ORBIT DETERMINATION RESULTS

Results from two simulations are presented in this section, denoted Simulation 1 and Simulation 2, which use observations of GEO objects from GTO and SSO-based optical sensors. Precise ephemerides of Galaxy 15 (WAAS 135) from May of 2010 are used in Simulation 1 with astrometric (right ascension and declination) measurements used for

---

[1] The blackbody temperature of the Sun is 5778 K. Integrating from 380 nm to 750 nm yields 43.8% of the total flux and integrating from 400 nm to 700 nm yields 36.7% of the total flux. Given this window, we use an average value of 40%.

orbit determination. Simulation 2 models a simulated sphere in GEO that is tracked with both astrometric and photometric (apparent magnitude) measurements. Orbit determination accuracies of both cases are analyzed using GTO and SSO surveillance platforms. Fig. 2 demonstrates the geometry between sensors, target, and Sun. Both sensors operate in a dedicated object tracking mode where the target object is tracked for 30 minutes each pass. All astrometric measurements are given zero mean Gaussian noise with a standard deviation of 0.5 arcseconds.
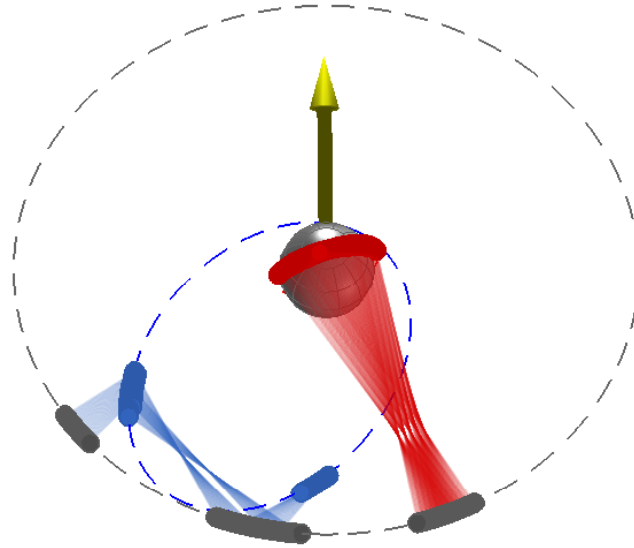

Fig. 2. Geometry of GTO (blue), SSO (red), and GEO (gray) orbits with marker dots indicating their locations when observations are made. The yellow arrow points towards the Sun.

The orbit determination process for both simulations utilizes an unscented Kalman filter (UKF) [32, 33]. A UKF uses a small number of sigma points generated about the mean state to capture the mean and covariance of a random variable, providing a representation that is guaranteed to be accurate to 2nd order. This process is referred to as the unscented transform. The UKF was chosen for this work because of the second order accuracy and the fact that it does not require the computation of Jacobians of measurement and dynamical models. The Jacobians needed in batch filters, conventional Kalman filters (CKF), and extended Kalman filters (EKF) increase in difficulty as more complex measurement types and state dynamics are incorporated. The UKF readily handles any kind of measurement or state with few changes to the code.

3.1. SIMULATION 1: ASTROMETRIC MEASUREMENTS OF GALAXY 15 (WAAS 135)

Simulation 1 is based on WAAS ephemerides for Galaxy 15 during the period of time when Galaxy 15 was uncontrolled in 2010[1]. During this time, 5 to 10-meter position accuracy of the satellite was still being achieved while drifting without stationkeeping maneuvers. These ephemerides are used to generate the baseline observations and serve as a reference trajectory for analyzing filter performance.

Astrometric measurements are taken every 20 seconds for a maximum of 30 minutes per pass. The schedule of the 3 passes of observations for both GTO and SSO sensors is depicted in Fig. 3. Observations from the GTO are made when the GTO sensor is above 30,000 km radius (23,600 km altitude) and when the phase angle is below 60 degrees. Similar phase angle constraints were placed on the SSO sensor. For this simulation, the UKF estimates Cartesian position and velocity as well as the coefficient of reflectivity with *a priori* standard deviations of 500 m, 2 m/s, and 0.1, respectively.

The force models implemented in the UKF are listed in Table 2. A spherical body is assumed for the solar radiation and Earth radiation pressure models since the exact attitude of Galaxy 15 is unknown.
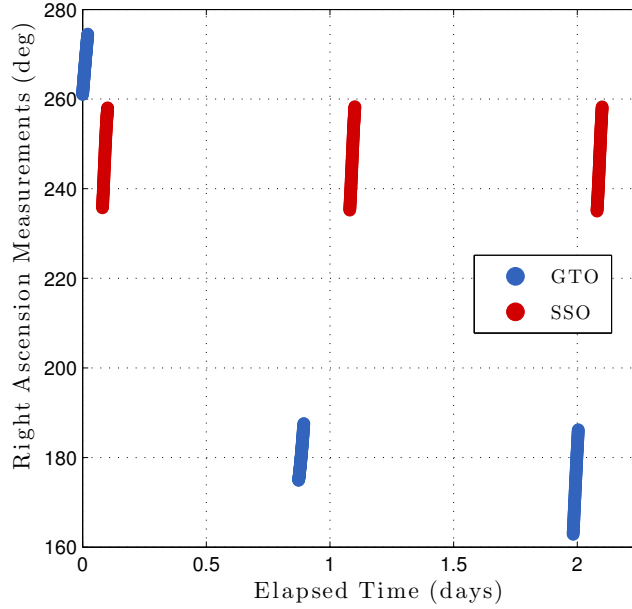
---

[1]http://www.nstb.tc.faa.gov/DisplayNSTBDataDownload.htm

Fig. 3. Right ascension measurements made by GTO and SSO sensors for Simulation 1.

Table 2. Summary of models used in UKF for Simulation 1.

Model	Type	References
Earth Gravity Field	10x10 EGM2008	[34]
Tides	permanent tide only	[35]
Third Body	Sun, Moon (JPL DE421)	[36]
Solar Radiation Pressure	spherical body, cylindrical shadow	[37]
Earth Radiation Pressure	spherical body	[38]
GCRF/ITRF	IAU 2006/ 2000A$_{R06}$	[35]
Earth Orientation Parameters	CelesTrak (IERS and NGA)	[35, 39]

Table 3. Final values of radial (R), in-track (I), and cross-track (C) position and velocity 1-σ covariance for Simulation 1. The full simulation involves 3 observation passes for each platform as shown in Fig. 3. The "2 passes" category indicates that only the first two passes of each sensor platform were used.

Component	Units	SSO	GTO	SSO + GTO (3 passes)	SSO + GTO (2 passes)
R (σ)	m	134.1	115.9	33.1	37.5
I (σ)	m	13.4	69.6	12.1	11.6
C (σ)	m	23.9	14.3	8.6	11.2
3D Position (σ)	m	136.8	135.9	36.2	40.8
3D Velocity (σ)	mm/s	107.6	35.8	4.9	4.6

The final 1-σ covariance for velocity and radial, in-track, and cross-track position estimates are given in Table 3. As standalone sensors, the GTO and SSO platforms perform similarly in position estimation, while velocity is estimated much better by the GTO. One might expect the GTO to perform significantly better on its own due to the decreased distance to target as compared to an SSO, however, the change in right ascension and declination measurements over time are much less than those made by an SSO. This decreased change over time is caused by the GTO sensor following

the GEO object, thus maintaining a similar viewing geometry over time. If the GTO observes the GEO object nearly along the GEO object's orbit (which happens when the GTO is near apogee and the GEO object is a few hours ahead), angles measurements result in an improved knowledge of the target's radial direction and a deterioration of in-track knowledge. This is evidenced by the radial and in-track standard deviations in Table 3. By combining measurements from both platforms, estimation of position and velocity is significantly improved over either standalone system. Even when cutting down the number of total observations to 2 passes each, the target state is estimated to a much higher fidelity than either standalone system with more observations. These results highlight the beneficial nature of including a GTO-based optical sensor into the current system monitoring the GEO belt.

3.2. SIMULATION 2: ASTROMETRIC AND PHOTOMETRIC MEASUREMENTS OF SPHERICAL DEBRIS

Simulation 2 consists of a target trajectory and observation schedule similar to that of Simulation 1, but with a fictitious spherical object as the GEO target and an additional 4th pass of observations. Measurements of apparent visual magnitude are now added to the right ascension and declination measurements to estimate position, velocity, cross-sectional area, and mass. All photometric measurements include zero mean Gaussian noise with standard deviations computed using Eq. (4). The dynamic model used in the UKF, reference trajectory generation, and observation generation assumes the target is a diffuse sphere. This is intended to be a test case to analyze the relative abilities of GTO and SSO sensors to estimate area and mass under ideal conditions. Table 4 lists the true value, initial error, and *a priori* 1-σ covariance values for mass and area.

Photometric measurements allow the filter to observe cross-sectional area as seen in Eq. (2). Mass, however, is not directly observed by either astrometric or photometric measurements. For objects in GEO, area and mass are only present in the acceleration due to solar radiation pressure, and to a much lesser extent Earth radiation pressure, in the term $C_r A/m$. We assume a constant value for C_r of 1.2 and observe area, leaving mass to be "estimated". In reality, mass will only be approximated because this term soaks up some error in the coefficient of reflectivity, area, attitude, shape, chosen bidirectional reflectance distribution function (BRDF), and other dynamic mis-modeling errors.

Dynamical systems sometimes include one or more state parameters that are limited in the values they can take on, possibly due to physical characteristics or the laws of physics. Cross-sectional area of a spacecraft is one example, with the constraint $A > 0$. The UKF (as well as the CKF, EKF, and batch) does not inherently contain a way of enforcing constraints. However, [40] presents a simple method for incorporating state constraints into the UKF. If a sigma point has a value for cross-sectional area, for example, that is less than zero, the area is forced to be slightly above zero before the next covariance is computed. The sigma points should be checked for these constraints each time new sigma points are generated. The final state parameter estimate must also be checked. This type of constraint is implemented in Simulation 2 for both mass and cross-sectional area.

Table 4. True and *a priori* values of mass and area for Simulation 2.

Property	True Value	Initial Value	Initial Std. Dev. (σ)
Mass	20 kg	500 kg	200 kg
Area	1.77 m^2	20 m^2	7 m^2

As mentioned previously, the uncertainty of each photometric measurement is determined by the signal-to-noise ratio of the target on the CCD. Fig. 4 illustrates the benefit of using a GTO for observing GEO. GTO-based photometric measurements will have a smaller uncertainty due to the higher signal-to-noise values.
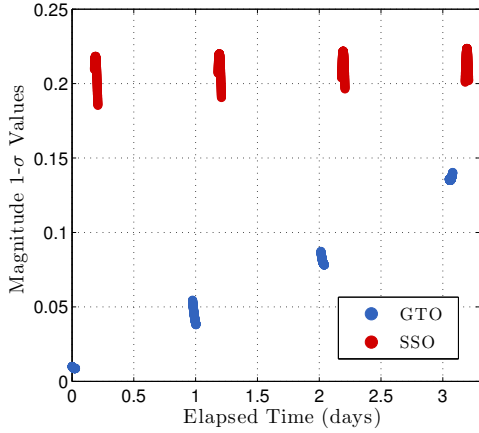
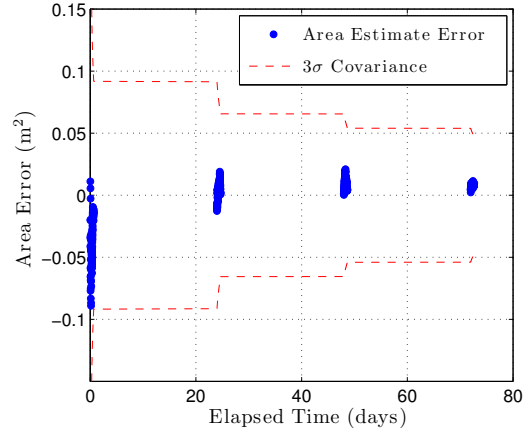Fig. 4. Standard deviations of apparent magnitude measurements from GTO and SSO platforms.

Fig. 5. Cross-sectional area estimation error and covariance from SSO observations.

Fig. 5 and 6 in addition to Table 5 display the mass and area estimation performance of GTO and SSO sensors. Both observation platforms estimate the cross-sectional area quickly and accurately. In part, this is due to the fact that both the truth trajectory and filter model utilize a spherical object. In reality, the estimation of area is difficult without also estimating attitude and shape. This is acceptable for this study, because Simulation 2 is meant to compare the relative estimation abilities of the two sensor platforms, not evaluate absolute estimation accuracy in a real world setting. Reference [41] discusses the difficulties of estimating area in greater detail.

For mass, the SSO platform has more difficulty as compared to the GTO. While the GTO nearly estimates the true mass by itself, the SSO sensor makes little progress in reducing the covariance. Note that in combination, the system reduces an initial 1-σ covariance of 200 kg down to almost 20 kg. This is a significant improvement over either standalone system performance.

(a) SSO
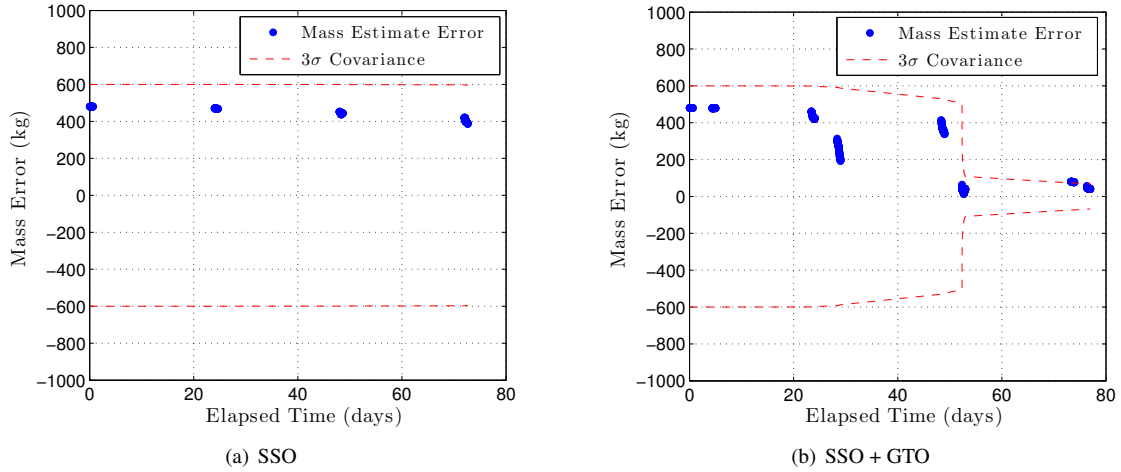

(b) SSO + GTO

Fig. 6. Mass estimation results for SSO only and SSO plus GTO.

Table 5. Final 1-σ covariance values for area and mass.

Component	Units	SSO	GTO	SSO + GTO
Area (σ)	m^2	0.016	0.001	0.001
Mass (σ)	kg	198.6	61.8	22.6

4. CONCLUSION AND DISCUSSION

In this paper, we present improved orbit determination of GEO objects through the use of a simulated optical sensor placed in a GTO, recording both astrometric and photometric measurements. Two simulated sparse tracking scenarios, using precise WAAS ephemerides and a fictitious spherical object, demonstrate that the combination of GTO and SSO-based measurements yields faster estimation and uncertainty reduction of states and physical properties than SSO alone.

By using precise WAAS ephemerides for Galaxy 15 during its uncontrolled state in 2010, we gain insight into achievable uncertainties with each SBSS platform and their combination. The difference in geometry of observing GEO from a GTO results in more radial information and improved velocity estimation compared to the traditional SSO. The combination of the two platforms yields a significant improvement to orbit determination, even in a sparse tracking scenario.

The second simulation consists of a small spherical object with photometric measurements being used in addition to angles measurements. This combination of measurement types allows the mass and area to be separately estimated in the filter. Photometric measurements allow for the cross-sectional area to be approximated. By assuming a fixed value for the coefficient of reflectivity, the object's mass can be approximated over time. While the GTO on its own is shown to reduce the target's mass uncertainty much faster than an SSO, the combination of the two surpass any standalone system, as might be expected.

Beyond the orbit determination results of this paper, previous research has demonstrated that these alternative SBSS orbits, such as GTO and sub-GEO, offer the capability of detecting GEO debris down to a couple of centimeters in diameter. Furthermore, a small GTO SBSS satellite could be launched as a secondary payload on a GEO launch, making the cost more attractive. While this brief study focused on using a GTO in concert with an SSO, future work will include the use of sub-GEO orbits for orbit determination in similar simulations. Future work will also include analyzing the estimation error of area and mass in the presence of attitude and shape mis-modeling for several SBSS platforms.

5. ACKNOWLEDGMENT

6. REFERENCES

1. E. Soop. *Handbook of Geostationary Orbits*. Kluwer Academic, Dordrecht, 1994.

2. Robert Scott and Brad Wallace. Small aperture telescope observations of co-located geostationary satellites. In *Advanced Maui Optical and Space Surveillance Technologies Conference (AMOS)*, Maui, HI, September 1-4 2009.

3. David A. Vallado. Verifying observational data for real world space situational awareness. In *AAS/AIAA Astrodynamics Specialist Conference*, AAS 11-439, Girdwood, AK, July 31-August 4 2011.

4. T. Schildknecht, R. Musci, M. Ploner, S. Preisig, J. de Leon Cruz, and H. Krag. Optical observations of space debris in the geostationary ring. In *Proceedings of the Third European Conference on Space Debris*, ESA SP-473, pages 89–94, Darmstadt, Germany, March 19-21 2001.

5. T. Schildknecht, R. Musci, M. Ploner, G. Beutler, W. Flury, J. Kuusela, J. de Leon Cruz, and L. de Fatima Dominguez Palermo. Optical observations of space debris in GEO and in highly-eccentric orbits. *Advances in Space Research*, 34:901–911, 2004.

6. T. Schildknecht, T. Flohrer, R. Musci, and R. Jehn. Statistical analysis of the ESA optical space debris surveys. *Acta Astronautica*, 63:119–127, 2008.

7. H. Krag, P. Beltrami-Karlezi, J. Bendisch, H. Klinkrad, D. Rex, J. Rosebrock, and T. Schildknecht. PROOF - the extension of ESA's MASTER model to predict debris detections. *Acta Astronautica*, 47(2-9):687–697, 2000.

8. H. Krag, J. Bendisch, H. Klinkrad, D. Rex, T. Rieger, J. Rosebrock, and T. Schildknecht. Debris model validation and interpretation of debris measurements using ESA's PROOF tool. *Acta Astronautica*, 48(5-12):373–383, 2001.

9. Holger Krag, J. Bendisch, H. Klinkrad, and P. Wegener. The extended PROOF tool - a sophisticated model for the simulation of debris measurement campaigns. In *52nd International Astronautical Congress*, IAA 01-6.4.04, Toulouse, France, October 1-5 2001.

10. H. Krag, M. Kahl, J. Bendisch, H. Klinkrad, and T. Schildknecht. Space based optical observation of small debris objects. In *Proceedings of the Third European Conference on Space Debris*, ESA SP-473, pages 147–152, European Space Operations Centre (ESOC), Darmstadt, Germany, March 19-21 2001.

11. Michael Oswald, Carsten Wiedemann, Peter Wegener, Marc Schluter, and Peter Vorsmann. Space-based radars for the observation of orbital debris in GEO. In *Space 2003*, AIAA 2003-6294, pages 1–10, Long Beach, CA, September 23-25 2003.

12. M. Oswald, H. Krag, P. Wegener, and B. Bischof. Concept for an orbital telescope observing the debris environment in GEO. *Advances in Space Research*, 34:1155–1159, 2004.

13. F.J.P. Wokke, A.J. Kramer, R. van Benthem, R.A. Annes, T. Flohrer, T. Schildknecht, E. Stöveken, E. Valtonen, J. Peltonen, E. Riihonen, T. Eronen, and J. Kuusela. An instrument design for space-based optical observation of space debris. In *56th International Astronautical Congress*, IAC-05-B6.1.08, 2005.

14. T. Flohrer, T. Schildknecht, R. Jehn, and M. Oswald. Performance of a proposed instrument for space-based optical observations of space debris. In *57th International Astronautical Congress*, IAC-06-B6.1.1, October 2-6 2006.

15. Moriba K. Jah and Ronald A. Madler. Satellite characterization: Angles and light curve data fusion for spacecraft state and parameter estimation. In *Advanced Maui Optical and Space Surveillance Technologies Conference (AMOS)*, Maui, HI, September 11-14 2007.

16. Richard Linares, John L. Crassidis, Moriba K. Jah, and Hakjae Kim. Astrometric and photometric data fusion for resident space object orbit, attitude, and shape determination via multiple-model adaptive estimation. In *AIAA Guidance, Navigation, and Control Conference*, Toronto, Ontario Canada, August 2-5 2010.

17. Richard Linares, Moriba K. Jah, and John L. Crassidis. Inactive space object shape estimation via astrometric and photometric data fusion. In *AAS/AIAA Space Flight Mechanics Meeting*, AAS 12-117, Charleston, SC, Jan. 30 - Feb. 2 2012.

18. Richard Linares, Moriba K. Jah, and John L. Crassidis. Space object area-to-mass ratio estimation using multiple model approaches. In *35th AAS Guidance, Navigation, and Control Conference*, AAS 12-015, Breckenridge, CO, February 2012.

19. Richard Linares, Moriba K. Jah, John L. Crassidis, Fred A. Leve, and Tom Kelecy. Astrometric and photometric data fusion for inactive space object feature estimation. In *62nd International Astronomical Congress*, IAC-11-A6.6.4, Cape Town, South Africa, October 2011.

20. Richard Linares, Fred A. Leve, Moriba K. Jah, and John L. Crassidis. Space object mass-specific inertia matrix estimation from photometric data. In *35th AAS Guidance, Navigation, and Control Conference*, AAS 12-014, Breckenridge, CO, February 2012.

21. Charles J. Wetterer. Attitude estimation from light curves. *Guidance, Control, and Dynamics*, 32(5):1648–1651, September-October 2009.

22. Jill Tombasco and Penina Axelrad. A study of the achievable geosynchronous angles-only orbit estimation accuracy. *Journal of the Astronautical Sciences*, 58(2):275–290, 2011.

23. Ian S. McLean. *Electronic Imaging in Astronomy: Detectors and Instrumentation*. Praxis Publishing Ltd, 2nd edition, 2008.

24. Gary A. McCue, James G. Williams, and Joan M. Morford. Optical characteristics of artificial satellites. Technical Report SD 70-55, North American Rockwell-Space Division, July 1970.

25. Henry Norris Russell. The stellar magnitudes of the sun, moon, and planets. *Astrophysical Journal*, 43:103–129, 1916.

26. R. Tousey. Optical problems of the satellite. *Journal of the Optical Society of America*, 47(4):261–267, April 1957.

27. Herbert Raab. Detecting and measuring faint point sources with a ccd. In *Proceedings of Meeting on Asteroids and Comets in Europe (MACE)*, Visnjan, Croatia, May 17-19 2002.

28. Estrella Olmedo, Noelia Sanchez-Ortiz, Nuria Guijarro, Jaime Nomen, and Holger Krag. Survey-only optical strategies for cataloguing space debris objects in the future European space surveillance system. *Advances in Space Research*, 48:535–556, 2011.

29. Alistair Walker. *N.O.A.O. Newsletter*, (10), 1987.

30. Jay Elias. *N.O.A.O. Newsletter*, (37), 1994.

31. Qiang Fu. Radiation (solar). In James R. Holton, John Pyle, and Judith A. Curry, editors, *Encyclopedia of Atmospheric Sciences*, pages 1859–1863. Academic Press, 2003.

32. Simon Julier and Jeffrey Uhlmann. A new extension of the Kalman filter to nonlinear systems. In *In Proceedings of AeroSense: The 11th International Symposium on Aerospace/Defence Sensing, Simulation and Controls*, 1997.

33. Simon Julier, Jeffrey Uhlmann, and Hugh F. Durant-Whyte. A new method for the nonlinear transformation of means and covariances in filters and estimators. *IEEE Transactions on Automatic Control*, 45(3):477–482, March 2000.

34. N.K. Pavlis, S.A. Holmes, S.C. Kenyon, and J.K. Factor. An Earth gravitational model to degree 2160: EGM2008. In *presented at the 2008 General Assembly of the European Geosciences Union*, Vienna, Austria, April 13-18 2008.

35. Gérard Petit and Brian Luzum. IERS technical note no. 36–IERS conventions (2010), 2010. Bureau International des Poids et Mesures and U.S. Naval Observatory.

36. W.M. Folkner, J.G. Williams, and D.H. Boggs. The planetary and lunar ephemeris DE 421. JPL Memorandum IOM 343R-08-003, Jet Propulsion Laboratory (JPL), March 2008.

37. David A. Vallado. *Fundamentals of Astrodynamics and Applications*. Published jointly by Microcosm Press and Springer, 4th edition, 2013.

38. Philip Knocke, J. Ries, and B. Tapley. Earth radiation pressure effects on satellites. In *AIAA/AAS Astrodynamics Specialist Conference*, Paper 88-4292-CP, Minneapolis, MN, August 1988.

39. D.A. Vallado and T.S. Kelso. Earth orientation parameter and space weather data for satellite operations. In *AAS/AIAA Space Flight Mechanics Meeting*, AAS 13-373, Kaui, HI, February 2013.

40. Rambabu Kandepu, Bjarne Foss, and Lars Imsland. Applying the unscented Kalman filter for nonlinear state estimation. *Journal of Process Control*, 18(7):753–768, 2008.

41. John Africano, Paul Kervin, Doyle Hall, Paul Sydney, John Ross, Tamara Payne, Steve Gregory, Kira Jorgensen, Kandy Jarvis, Tracy Parr-Thumm, Gene Stansbery, and Ed Barker. Understanding photometric phase angle corrections. In *Proceedings of the 4th European Conference on Space Debris*, pages 141–146, Darmstadt, Germany, April 18-20 2005.